ROYAL SOCIETY OF CHEMISTRY

EDGE ARTICLE

Check for updates

Support morphology-dependent alloying behaviour and interfacial effects of bimetallic Ni–Cu/CeO₂ catalysts†

Yanan Liu, [ID] [ab] Alan J. McCue, [ID] [c] Pengfei Yang, [ID] [ab] Yufei He, [ID] [ab] Lirong Zheng, [ID] [d] Xingzhong Cao, [ID] [d] Yi Man, [ID] [e] Junting Feng, [ID] *[af] James A. Anderson [ID] *[c] and Dianqing Li [ID] [ab]

The impregnation method is commonly employed to prepare supported multi-metallic catalysts but it is often difficult to achieve homogeneous and stable alloy structures. In this work, we revealed the dependence of alloying behavior on the support morphology by fabricating Ni–Cu over different shaped CeO₂. Specifically, nanocube ceria favoured the formation of monometallic Cu and Ni-rich phases whereas polycrystalline and nanorod ceria induced the formation of a mixture of Cu-rich alloys with monometallic Ni. Surprisingly, nanopolyhedron (NP) ceria led to the generation of homogeneous Ni–Cu nanoalloys owing to the equivalent interactions of Ni and Cu species with CeO₂ (111) facets which exposed relatively few coordinative unsaturated sites. More importantly, a strong interfacial effect was observed for Ni–Cu/CeO₂-NP due to the presence of CeOₓ adjacent to metal sites at the interface, resulting in excellent stability of the alloy structure. With the aid of CeOₓ, NiCu nanoalloys showed outstanding catalytic behaviour in acetylene and hexyne hydrogenation reactions. This study provides valuable insights into how fully alloyed and stable catalysts may be prepared by tailoring the support morphology while still employing a universal impregnation method.

Introduction

The growing demand for energy-efficient industrial processes requires next generation catalysts to deliver higher activity and selectivity with long lifetimes. Alloys have been often preferred over single metals in many important applications as they demonstrate distinct properties compared to the parent metals.[1,2] Concerning strategies for synthesis, it is well known that conventional impregnation has been historically employed to fabricate catalysts in industry, but there is a continuing challenge to achieve homogeneous alloy structures for multi-component systems.[3,4] Recently, Christopher's group[5] showed that the Al₂O₃ support had a more pronounced effect on the construction of alloys than TiO₂ in the impregnation

methodology, which provided the possibility for us to develop well-controlled structures by precise regulation of support properties even when the traditional preparation process was employed.

As one of the most fascinating rare earth oxides, ceria (CeO₂) has been extensively employed in a variety of applications, including catalysis,[6–8] fuel cells[9] and oxygen sensors[10] due to its unique properties and remarkable performance. On account of recent developments in the fabrication of nanomaterials, ceria with controllable facets may be successfully achieved, and thus the influence of specific facets of CeO₂ in the field of catalysis was recently explored in depth.[11,12] Some proposals discovered that in virtue of the different atomic arrangements and the dissimilarity in surface oxygen vacancies, distinct crystal planes of CeO₂ present different reactivities for surface oxygen,[13,14] and strongly affect the dispersion,[15–17] morphology,[18–20] and electronic environment[21–23] of active metals in single metal systems. However, studies regarding the influence of CeO₂ crystal planes on bimetallic structures have not been reported. Generally speaking, the degree of segregation/mixing in bimetallic AₘBₙ/S catalysts primarily relies on the relative strengths between metal–metal and metal–support.[1,2] If A–B bonds are strongest with equal strength of A–S and B–S bonds, this favours mixing; otherwise, segregation is preferred. Given the impact of support properties on the bond strength, it prompts us to explore the dependence of alloying behavior on the support morphology

[a] State Key Laboratory of Chemical Resource Engineering, Beijing University of Chemical Technology, Beijing, China. E-mail: fengjt@mail.buct.edu.cn

[b] Beijing Engineering Center for Hierarchical Catalysts, Beijing University of Chemical Technology, Beijing 100029, China

[c] Surface Chemistry and Catalysis Group, Department of Engineering, University of Aberdeen, Aberdeen, UK. E-mail: j.anderson@abdn.ac.uk

[d] Institute of High Energy Physics, Chinese Academy of Sciences, Beijing, China

[e] Beijing Research Institute of Chemical Industry, Sinopec Group, Beijing, China

[f] Beijing Advanced Innovation Center for Soft Matter Science and Engineering, Beijing University of Chemical Technology, Beijing, China

† Electronic supplementary information (ESI) available: Fig. S1–S21, Tables S1–S9. See DOI: 10.1039/c8sc05423a

and thus establish a novel and universal route to prepare well-alloyed catalysts simply by controlling the support morphology.

Previously, it has been well documented that ceria can stabilize monometallic nanoparticles due to its reducibility that readily generates a strong interfacial anchoring effect.[18] Furthermore, this effect could stabilize single atom catalysts allowing for high thermal stability as reported by Jones[6] and Liu groups.[24] In terms of bimetallic systems, except for the stability of size, maintenance of the distribution of two different metallic elements within a structure is still a challenging task, mainly lying in the prevention of dealloying inherently caused by the reaction temperature[25] or reactants.[26,27] Given the ability of ceria to improve the stability of single metals at the atomic level, it inspired us to try to utilize the interfacial effect, highly sensitive to the ceria structure, to enhance the stability, especially the arrangement and distribution of the two metallic elements. Considering both previously mentioned historical problems, simultaneously constructing well-defined and highly stable alloys only by regulating the support morphology could be of great significance.

Herein, in this work, we first explore and put forward the support morphology/facet-dependent alloying behaviour as well as interfacial effects. In detail, a series of CeO_2 materials with nanopolyhedron (NP), nanorod (NR), nanocube (NC) and conventional polycrystalline (CV) shapes were fabricated and used as supports to achieve environmentally benign non-noble Ni–Cu catalysts by conventional impregnation. As expected, different morphologies over substrates indeed impact significantly the atomic distribution and stability of active components, as confirmed by XPS, XAS and Cs-corrected STEM. CeO_2-NP mainly involving (111) facets contributes to the formation of a homogenous and stable NiCu alloy with a strong interfacial effect originating from CeO_x species, whereas nanocube ceria with (100) facets induces the formation of mixtures of monometallic Cu and Ni-rich phases. The nature of how ceria morphology influences the metal alloy is revealed. The well-defined and stable NiCu alloy adjacent to the CeO_x surface exhibits the best catalytic performance in the selective hydrogenation of acetylene and hexyne, and the structure–performance relationships are elaborated by a combination study based on *in situ* DRIFT and chemisorption. This study not only supplies an innovative strategy for fabricating stable and highly alloyed catalysts, but also reveals the essence of the support morphology dependent structure–property relationship.

Results and discussion

Characterization of the support morphology and structure

A series of shape-controlled CeO_2 nanocrystals and conventional CeO_2 were fabricated by hydrothermal treatment. The crystalline structures and shapes were confirmed by XRD (Fig. S1†) and HRTEM (Fig. 1) with good agreement between the observed reflection profiles, lattice parameters (Table S1†) and those reported in ref. 12–23. In detail, CeO_2-CV possesses a polycrystalline structure, which is usually described as a sphere-like shape with various exposed facets including (200), (111) and (220). For CeO_2-NP, it preferentially exposes (111)
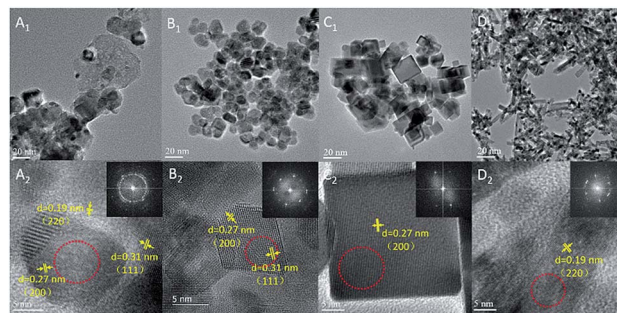

Fig. 1 HRTEM of (A) CeO_2-CV, (B) CeO_2-NP, (C) CeO_2-NC, and (D) CeO_2-NR. The SAED pattern areas are recorded from the area marked by the red circle.

facets, while the dominant (200) facets exist in CeO_2-NC.[11,28] In terms of nanorod ceria, a domain oriented along the [110] direction is observed. However, very recently, it was reported that ceria rods underwent extensive restructuring at certain temperatures, leading to the exposure of (111)-oriented surface regions resulting from faceting of the {110} plane.[29]

Likewise, it was also found that CeO_2-NC had a contribution from {110} and {111} facets, which increased with calcination temperature. To obtain the proof of nature of facets and the estimated proportion of exposed facets, statistics from Cs-corrected STEM analysis are obtained by counting more than 100 particles for each sample. The ratio of the (111) facet involved in the polyhedron is *ca.* 90% with 10% of (100) facets, while about 80% of (100) facets with 15% of (110) facets and small amount of (111) facets are observed in CeO_2-NC. In terms of nanorod ceria, *ca.* 50% of (110) facets with 30% of (111) and 20% of (100) facets are involved. For CeO_2-CV polycrystalline, it contains *ca.* 33% of (111), 35% of (100) and 32% of (110) facets.

It is well known that different exposed crystal surfaces could cause different properties such as surface stability, resulting in a different number of low coordination sites, which were recently investigated using methanol adsorption and FTIR.
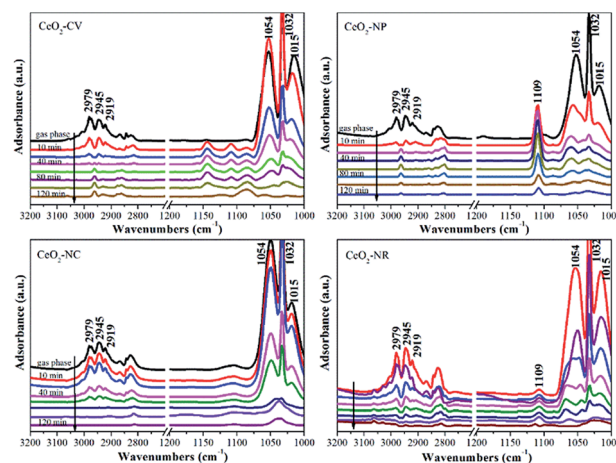

Fig. 2 Methanol-IR spectra on different shaped ceria materials after exposure to He at room temperature for 10 min, 20 min, 40 min, 60 min, 80 min, 100 min and 120 min, respectively.

Fig. 2 presents the methanol spectra of CeO_2 samples collected after exposure to He from 10 min to 120 min at room temperature. As expected, in the spectrum of each CeO_2 sample, the peaks of gas phase/physisorbed methanol at 1054 and 1015 cm^{-1} assigned to the C–O stretching and at 2978, 2945, and 2919 cm^{-1} ascribed to the C–H stretching basically disappear after 120 min sweeping.[30] However, the peak at 1032 cm^{-1} still remains, which could be ascribed to the residual physisorbed methanol or chemisorbed bridging methoxy species which is coincidently overlapped with the former one. To further rule out physisorbed methanol species, the samples were heated in He at 120 °C (Fig. S2†). After the treatment at high temperature, the peak at $ca.$ 1032 cm^{-1} has not disappeared, demonstrating that it should be attributed to chemisorbed methoxy species. In the absence of gas phase/physisorbed methanol, obvious distinctions in the chemisorption of methanol including on-top methoxy (1109 cm^{-1}), bridging methoxy and three-coordinate methoxy (1054–1015 cm^{-1}) are noticed in these samples. The ratio of linear to multi-coordinate methoxy species increases in this order: CeO_2-NC < CeO_2-NR < CeO_2-NP < CeO_2-CV, reflecting a few unsaturated sites existing in the truncated polyhedron, while more coordinatively unsaturated sites exist in the rod and cube ceria, which is in agreement with the literature.[11] To further confirm this above conclusion, $in\ situ$ Raman spectroscopy was employed. As shown in Fig. S3,† the feature band ascribed to the 2LO mode of ceria is observed at 1174 cm^{-1}.[31]

Once exposed in the environment with methanol, additional peaks appear, in which the ones at 1106, 2815, and 2922 cm^{-1} are owing to on-top methoxy, the peak at 1037 cm^{-1} is ascribed to bridging methoxy, and the peaks at 2844 and 2952 cm^{-1} are assigned to physisorbed methanol. As expected, in the process of desorption, the bands of physisorbed methanol obviously decrease, while the peaks of chemisorbed methanol still remain. Relative to the CeO_2-CV and CeO_2-NP mainly with on-top methoxy species, a higher ratio of multi-coordinate to linear methoxy species is observed in the CeO_2-NR and CeO_2-NC, which is in agreement with IR results.

Characterization of the catalyst structure

Surface termination of ceria with specific exposed planes plays a key role in the nature of single metal nanoparticles, as it shows the distinct redox capability and concentration of defects. However, the unambiguous identification of this type of function in a bimetallic system is unheard of, and thus support morphology-dependent properties of the active components are first explored. As shown in HRTEM (Fig. S4†) and CO-chemisorption (Table S2†),[32,33] the Ni–Cu particle size clearly displays slight differences in the sequence of CeO_2-NP (2.6 nm) < CeO_2-NC (3.4 nm) ≈ CeO_2-NR (3.5 nm) < CeO_2-CV (4.3 nm), while the metal dispersion follows the opposite trend. Fig. 3 exhibits the XRD patterns of all four catalysts. The errors of determination are also derived from five measurements (Fig. S5†), indicating that the data are accurate and effective. It is found (Fig. 3A) that a strong diffraction peak at 43.5° with a weak feature at 50.6° is located between the diffraction of monometallic Ni (JCPDS 04-0850) and Cu (JCPDS 04-0836) but close to Cu. Notably, a small
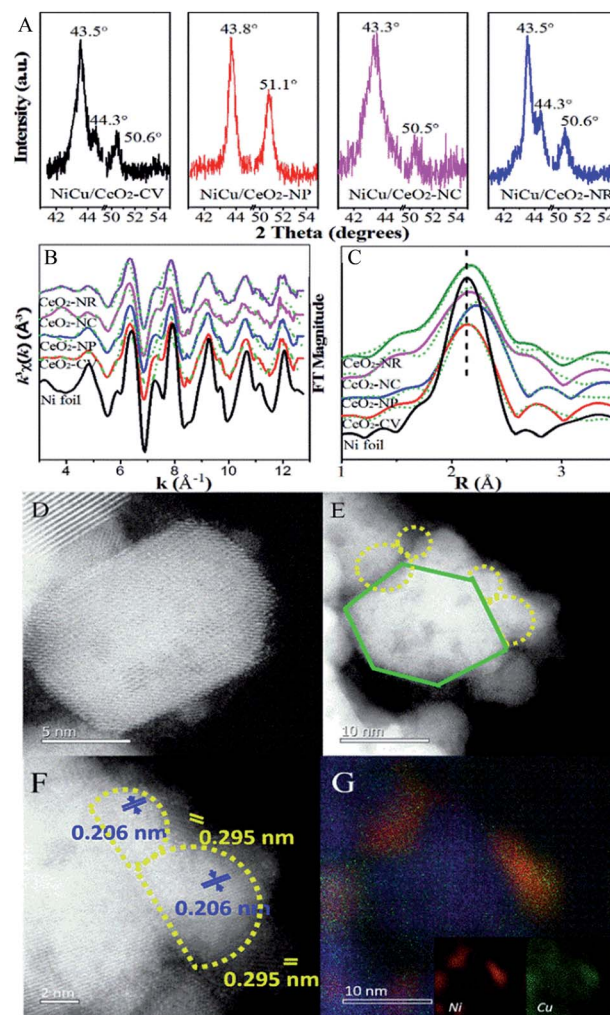

Fig. 3 (A) XRD profiles; (B) k^3-weighted Ni K-edge EXAFS oscillations; (C) Fourier transform spectra of CeO_2 supported Ni–Cu catalysts; (D–F) Cs-corrected STEM and (G) elemental mapping of Ni–Cu/CeO_2-NP.

shoulder appears at 44.3° indexed to diffraction from the Ni (111) facet. This suggests the formation of Cu rich nanoalloys with monometallic Ni in Ni–Cu/CeO_2-CV and Ni–Cu/CeO_2-NR. For the CeO_2-NP supported catalyst, two peaks at 2θ of 43.8° and 51.1° are observed without any other peaks, illustrating the existence of homogeneous NiCu nanoalloys, while the characteristics of the Cu phase are found at 43.3° and 50.5° along with some small peaks in the cubic CeO_2 system, implying the coexistence of monometallic copper and additional components including bimetallic NiCu nanoparticles as well as copper oxide. Considering that the mean particle size of Ni–Cu catalysts in our systems is close to the detection limitation of sampling, the XRD results could be only considered as the auxiliary proof. Thus, the local structure of NiCu nanoparticles is further discussed from the k^3-weighted Ni K-edge EXAFS oscillations and the corresponding Fourier transforms (Fig. 3). The fitting parameters including the bond lengths were summarized (Table S2†). Given the disparity between Ni foil (2.49 Å) and Cu foil (2.55 Å), the change of atomic distances in this work is not negligible. In detail, the atomic distances of

bimetallic NiCu systems increase *ca.* 0.2–0.5 Å, compared with the Ni foil (2.49 Å). The only explanation for the increase in Ni–Ni bond distance is that the Cu atoms effectively dilute continuous Ni sites.[34] Notably, Ni–Cu/CeO₂-NP exhibits the largest Ni–Ni bond distance of 2.54 Å, meaning that Ni sites in NiCu/CeO₂-NP are better isolated by Cu than the other three catalysts.

To further corroborate this structural analysis of active phases more conclusively and unambiguously, Cs-corrected HAADF-STEM was used to characterize the configuration of Ni–Cu/CeO₂-NP and Ni–Cu/CeO₂-NC given the obvious structural differences. Due to the much higher atomic number (Z) of Ce in comparison to Ni and Cu, the contrast of the latter in small size could not be effectively distinguished from the thickness effect of CeO₂ in the HAADF-STEM mode (Fig. 3D–F). By closely magnifying the TEM images (Fig. 3F), lattice fringes throughout the determined Ni–Cu particle are observed, with a distance of 0.206 nm, which is between that of Ni and Cu. However, considering the accuracy of lattice fringe measurements in STEM images, this may not be convincing evidence to certify the formation of nanoalloys. Additionally, a continuous crystalline lattice with a lattice spacing of 0.295 nm was also found which is assigned to reducible Ce species (PDF 44-1086). To further obtain more convincing evidence, EDX elemental mapping was performed in several zones to ensure analyses were representative. The corresponding results (Fig. 3G and S6†) confirm that Cu and Ni elements are homogeneously distributed at the nanometer scale over the polyhedron CeO₂ with Ni/Cu ratios of 48 : 52. For the Ni–Cu/CeO₂-NC, the distribution of Ni and Cu atoms exhibits several different trends with monometallic Cu and Ni-rich bimetallic nanoparticles (Fig. S6†), while polycrystalline and nanorod CeO₂ induced a mixture of Cu-rich alloys with monometallic Ni nanoparticles.

Insight into support facet-dependent alloying behaviour and interfacial effects

As expected, the properties of bimetallic components, in particular alloying behaviour were dependent on the support morphology; that is, Ni and Cu atom arrangements on the ceria with distinct crystal facets are noticeably different. This inspired us to focus on the exploration and understanding of the substrate morphology which induced alloying behaviour. According to the literature,[35,36] the degree of segregation/mixing and atomic order in A_mB_n/S bimetallic catalysts depend mainly on the relative strengths between metal–metal and metal–support, which are therefore explored by XRD measurement primarily. The measured lattice parameters of NiCu precursors are listed in Table S3,† with the estimated relative errors (Fig. S7†). Small error of the measurement confirms that the differences are significant. After calcination of the precursors, the decrease in various degrees of lattice parameters is seen in the nanocube and nanorod supported metal systems, but without any change noted in the Ni–Cu/CeO₂-NP-C500 and Ni–Cu/CeO₂-CV-C500 relative to the pristine ceria. This phenomenon is driven by the similarity in the radius of the Ni²⁺ cation (r = 0.85 Å) and Cu²⁺ cation (0.92 Å), which is more likely to form

NiCuOₓ as the alloy precursor in the process of calcination without any effect on the lattice parameters.[35,36] However, due to the large number of oxygen vacancies in the CeO₂-NR and CeO₂-NC, Ni²⁺ and Cu²⁺ ions enter more easily the lattice of CeO₂ in the process of calcination, leading to the formation of a NiCuCeOₓ solid solution in the bulk including (–Ni²⁺–O²⁻–Ce⁴⁺–) or (–Cu²⁺–O²⁻–Ce⁴⁺–) linkages, which are responsible for the decrease in the lattice parameters of ceria. Noticeably, combined with the well-known stronger interactions between Ni and CeO₂ compared to Cu²⁺ linked Ce⁴⁺,[5] it is speculated that the (–Ni²⁺–O²⁻–Ce⁴⁺–) linkage is more likely preferentially produced in our situation. Here, Ni K-edge EXAFS of the polyhedron and cube ceria which exhibit marked parametric variation is displayed to confirm the formation of the Ni–O–Ce structure. From the R space plot for Ni–Cu/CeO₂-NC-C500 (Fig. 4A and B), the first Ni–O shell possesses a distance of 2.15 Å, larger than that of Ni–Cu/CeO₂-NP-C500 (2.11 Å) and 2.08 Å observed for NiO (Table S3†), indicating Ni interaction with Ce in addition to Cu.

To provide evidence to support this proposal, TPR analysis of the precursors was performed. For the H₂-TPR profiles (Fig. 4C) of monometallic catalysts, Cu/CeO₂-CV-Pre exhibits a single reduction peak at 191 °C, while two peaks are observed for Cu/CeO₂-NP-Pre, Cu/CeO₂-NC-Pre and Cu/CeO₂-NR-Pre at 127 and 192 °C. The former is attributed to the reduction of CuO
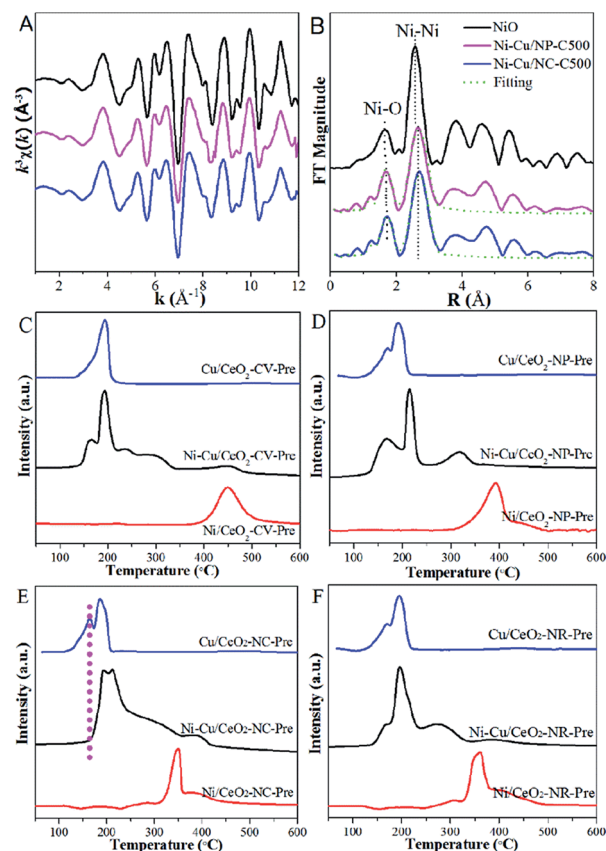

Fig. 4 (A) k^3-weighted Ni K-edge EXAFS oscillations, (B) Fourier transform spectra and (C–F) TPR of precursors.

interacting with CeO_2, whereas the latter is ascribed to the reduction of CuO.[5] However, no obvious peak due to the reduction of surface CeO_2 appears (at 480 °C for CeO_2). For the monometallic Ni system, a similar observation is obtained in CV, which shows only one reduction peak observed at 450 °C, associated with NiO reduction. TPR profiles over the precursors of different shaped CeO_2 supported Ni in Fig. 4D–F display two peaks at *ca.* 350 and 420 °C. The one at 350 °C originating from NiO strongly interacts with CeO_2, and the peak at 420 °C is due to the surface oxygen reduction of CeO_2. Compared with pure CeO_2, the shift in the temperature of reduction over different shaped CeO_2, particularly nanocube and nanorod (Fig. 4E and F), offers convincing evidence for significant interactions between CeO_2 and Ni. More importantly, the interaction of the support with Ni is stronger than that with Cu as judged by comparison of the shift in temperatures in the monometallic systems. With regard to bimetallic samples, the reduction peaks corresponding to Cu and Ni in polyhedron catalysts both move to lower temperatures (relative to the monometallic catalysts), which may be interpreted as the combination of Ni and Cu interactions as well as those between the metal and support. In terms of the other three substrate supported Cu–Ni species, the dominant signatures are assigned to the reduction of CuO (at *ca.* 190 °C) and NiO directly interacting with CeO_2 (at 210–290 °C). However, the reduction of CuO interacting with the support (at *ca.* 130 °C) in Ni–Cu/CeO_2-NR-Pre and Ni–Cu/CeO_2-CV-Pre is weak, and even absent in Ni–Cu/CeO_2-NC-Pre, clearly indicating stronger Ni–CeO_2 interactions than those of Cu, especially in Ni–Cu/CeO_2-NC-Pre. To better understand the reduction process, the corresponding quantitative information of TPR was provided. Calculation of H_2 uptake indicates the consumption of 1547–1862 μmol H_2/g over four samples, higher than 1497 μmol H_2/g expected for the reduction of NiO and CuO to the corresponding metal state. The difference of H_2 consumption can be accounted for by the reduction occurring not only on the metals but also on the support. Additionally, the TPR profiles are divided into several regions to confirm the reliability of the assignment for reduction peaks (Fig. S8 and Table S4†). The moles of consumed H_2 derived from zones 1 and 2 closely match with that for complete reduction of CuO and NiO, respectively, indicating that the assignment of the reduction peaks is reasonable. Moreover, relative to the CeO_2-CV, CeO_2-NC and CeO_2-NR systems, the CeO_2-NP supported NiCu system exhibits the highest H_2 consumption for the reduction of CeO_2 (zone 3), indicating that CeO_2 is easier to reduce with the aid of the NiCu alloy in the polyhedron.

Fig. 5, S9 and S10† show Cu 2p, Ni 2p and Ce 3d XP spectra of mono- and bimetallic catalysts. Since these catalysts were measured *ex situ*, contact with air in the process of transfer could cause the oxidation of metal. First, by analysing the Ni and Cu XPS spectra of monometallic catalysts (Fig. S9A†), it is noted that the change of the Ni^0 $2p_{3/2}$ peak over monometallic Ni samples on CeO_2-NR (0.4 eV), CeO_2-CV (0.3 eV), and particularly CeO_2-NC (0.5 eV) is more pronounced relative to that of Cu^0 in the corresponding monometallic Cu catalysts (*ca.* 0.2 eV), indicative of a stronger electronic interaction at the Ni–CeO_2 interface. Interestingly, the extent of the shift in the BE of the Ni
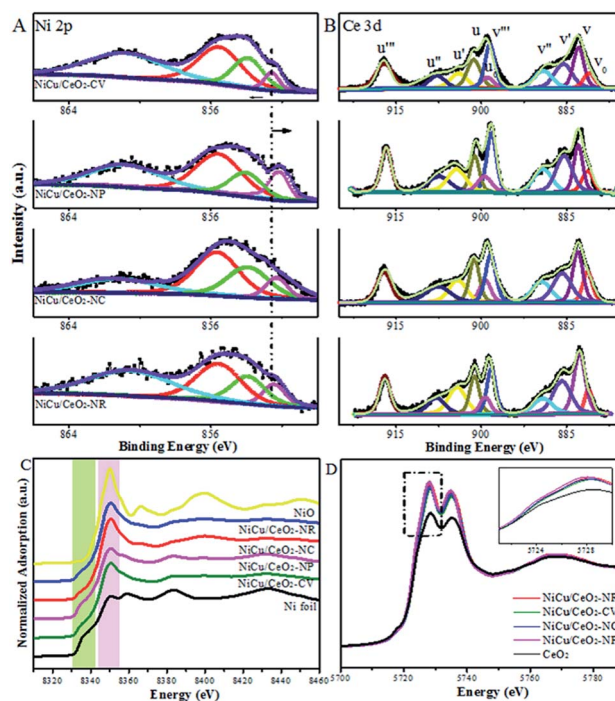

Fig. 5 XPS spectra of (A) Ni 2p and (B) Ce 3d. (C) Ni K-edge and (D) Ce L3-edge XANES spectra of all catalysts.

2p peaks is very similar to that observed for the Cu 2p signals in the case of the CeO_2-NP supported monometallic catalysts, revealing the close interplay of the substrate to Ni and Cu. Furthermore, with the introduction of Ni into the Cu samples, more metallic copper is obtained (Fig. S10†), suggesting that interaction between Ni and Cu species exists. However, no obvious change in the BE of copper within the bimetallic materials is detected, although the effect of Ce^{3+} and Ni on the nature of the Cu species is evident from the XPS data in Fig. S9 and S10.† This apparent contradiction can be rationalized on the basis of the electronic shifts arising from the electronegativity of all three components. In Ni XP spectra, Ni–Cu/CeO_2-NP with the lowest BE reflects the maximum electron density over Ni species under the combined effect of Cu and Ce^{3+} species (Fig. 5A). The combined study of XAS, TPR and XPS suggests homogeneous alloying over Cu–Ni/CeO_2-NP, while Cu atoms are readily separated and exposed at the surface of the other catalysts. Note that the spectra of Ce 3d (Fig. 5B) are fairly complex since a mixture of both Ce^{4+} and Ce^{3+} oxidation states exists, which is expected due to the formation of Ce^{3+} species with oxygen vacancies on the surfaces of the reduced catalysts, affirming the preliminary conclusion from STEM analysis. The six peaks denoted as v (882.8 eV), v″ (889.0 eV), v‴ (898.4 eV), u (901.2 eV), u″ (907.6 eV) and u‴ (917.0 eV) belong to CeO_2, while another four peaks labelled as v^0 (880.8 eV), v′ (885.6 eV), u^0 (898.9 eV) and u′ (904.0 eV) are characteristic of Ce_2O_3.[33,37] For Ni–Cu/CeO_2-NP, the abundance of Ce^{3+} (39.6%) is higher than that of the other three materials, indicating that the reduction of ceria is promoted by the presence of the metal, and the existence of a strong interaction between the active metal and ceria.

The normalized Ce L3-edge XANES profiles for Ni–Cu/CeO$_2$ materials in Fig. 5D present a double absorption feature at 5730 and 5737 eV. In comparison with the reference CeO$_2$, shifts are observed in the absorption edges towards lower energies for Ni–Cu samples but these are still close to the edge position of the standard CeO$_2$, implying the transformation from Ce^{4+} to Ce^{3+} but with Ce^{4+} species dominating in all samples.

The percentage of Ce^{3+} in Ni–Cu/CeO$_2$ in all four cases is significantly different, of which the polyhedron supported NiCu nanoalloy possesses the highest at 35%, based on the linear combination fit (LCF) using the Athena software.[38] Combined with the Raman and positron annihilation spectroscopy (PAS) analysis of reduced catalysts in Fig. S11B, Tables S5 and S6,† these results reveal the assistance of the NiCu alloy (hydrogen dissociation) for the generation of oxygen vacancies, which contributes to the strong interfacial effect. As shown in the normalized Ni K-edge XANES spectra (Fig. 5C), Ni–Cu/CeO$_2$-NC and Ni–Cu/CeO$_2$-NR present a stronger white line, whereas that in the polyhedron supported Ni–Cu is close to the Ni foil; however, a significant pre-edge feature similar to the Ni foil is clearly present in the spectra of these four catalysts. The above results suggest the existence of a NiO phase in these catalysts but the metallic state Ni is still predominant. This kind of Ni–O interaction may be caused by re-oxidation or Ni atoms strongly interacting with the support. Notably, a shift in the absorption edge toward lower photon energies compared to the Ni foil is observed, revealing that the Ni electronic density increases. This could be associated with the electron transfer from Ce^{3+} to metal atoms at the interface given no prominent change is noticed in Cu spectra (Fig. S12†). The spectroscopic results give a deeper understanding of the strong interfacial effect between the interfacial metal atoms and Ce^{3+}–O$_v$ sites. According to the above analysis, a possible mechanism of substrate morphology inducing the structure of the active metal is given in Scheme 1. To obtain universal information on the CeO$_2$ morphology-dependence, other metal alloys such as CeO$_2$-NP supported Ni–Co, Cu–Co, Ni–Ga and Cu–Ga catalysts were prepared. XRD

results (Fig. S13†) preliminarily confirm that Ni–Ga/CeO$_2$-NP possesses an alloy structure, indicating that the control of the CeO$_2$ shape might be extended to prepare other metal systems. Further research will be performed in the future work.

Catalytic behaviour

The hydrogenation of alkyne follows a consecutive reaction pathway with many parallel reactions that can drive the formation of undesired products,[39] and thus achieving a high selectivity at full conversion is still a challenge. The Ni–Cu/CeO$_2$ catalysts with the different morphologies were tested in the gas phase hydrogenation of acetylene using 4 equivalents of H$_2$ relative to acetylene. The lack of conversion of acetylene over pristine CeO$_2$ (Fig. S14B†) rules out any contribution of supports to the catalytic behavior under our testing conditions. Surprisingly, complete consumption of acetylene (Fig. S14A†) is observed for Ni–Cu/CeO$_2$-NP at 100 °C, while the conversion of the other three catalysts is only <70%, showing that these nanopolyhedron supported Ni–Cu materials are highly active. Turnover frequency (TOF) is a vital metric to assess the intrinsic activity. In this study, TOF is defined as the rate of converted acetylene per number of active sites which are assumed as exposed Ni atoms at low conversion (<15%) since Cu atoms are inactive at low temperature. Mass or heat transfer effects are ruled out by analysis of Weisz–Prater and Mears criteria (Table S7†). As for the intrinsic activity (Table S2†), a TOF of 0.0070 s^{-1} is achieved over Ni–Cu/CeO$_2$-NP, higher than the values for the other three catalysts, demonstrating that the structure of Ni–Cu/CeO$_2$-NP can effectively enhance catalytic activity. In terms of selectivity, the four catalysts exhibit similar product distribution with ethene being always the predominant product (Fig. 6A). When the conversion is 90%, the ethene selectivity improves dramatically from 55% (Ni–Cu/CeO$_2$-NC) to 70% (Ni–Cu/CeO$_2$-CV and Ni–Cu/CeO$_2$-NR) and then to the maximum 85% (Ni–Cu/CeO$_2$-NP). As is well known for the hydrogenation of acetylene, the selectivity at >99.5% conversion is a greater
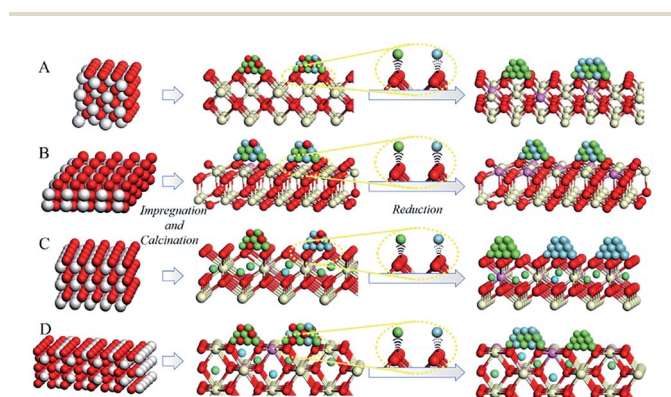
Scheme 1 The possible mechanism of the effect of support morphology on the structure of active metal in the preparation process from CeO$_2$ supports to Ni–Cu/CeO$_2$-C500 via the impregnation and calcination, and then to Ni–Cu catalysts via reduction over (A) CeO$_2$-CV, (B) CeO$_2$-NP, (C) CeO$_2$-NC and (D) CeO$_2$-NR supported Ni–Cu samples (white: Ce^{4+}; pink: Ce^{3+}; red: O; green: Ni; blue: Cu).
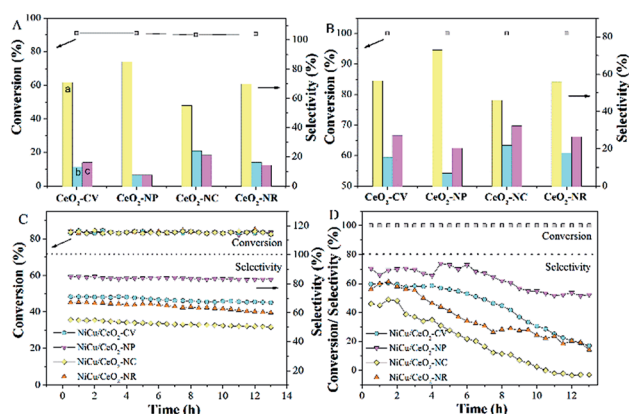

Fig. 6 Conversion of acetylene and product selectivity to ethylene (a; yellow), ethane (b; cyan) and oligomers (c; pink) at (A) low acetylene conversion and (B) full acetylene conversion; stability at (C) low acetylene conversion and (D) full acetylene conversion (0.1 g catalysts; 0.6% C$_2$H$_2$/5.4% C$_2$H$_4$/balance N$_2$; 4-fold excess of H$_2$; space velocity of 98 500 h^{-1}; 1 bar; 90–180 °C).

challenge and more relevant to the industrial process. Therefore, we further evaluate the selectivity at 100% conversion. The maximum selectivity to ethene (73.0%) is still achieved over Ni–Cu/CeO$_2$-NP, and is superior to those of the reported Ni-based materials and only slightly lower than those of state of the art materials such as ceria (81% sel. at 86% conv. −250 °C),[40] indium oxide (≈90% sel. at 30% conv. −350 °C),[41] and Pd$_4$S catalysts (94% sel. at 100% conv.-250 °C)[42] obtained at higher space velocity and hydrogen/acetylene ratios (Table S8†).

Interestingly, when Ni–Cu/CeO$_2$-NP-C500 was treated at 320 °C based on TPR (even though Ni–Cu/CeO$_2$-NP is also reduced at 250 °C but without good alloy structure in Fig. S15 and S16†), Ni–Cu/CeO$_2$-NP-R320 possesses a similar structure to Ni–Cu/CeO$_2$-NP-R500 as confirmed by XRD, but exhibits poor selectivity. Linking this performance and structure of Ni–Cu/CeO$_2$-NP-R500, a reasonable conclusion can be reached that the sites of the NiCu nanoalloy adjacent to CeO$_x$ at the interface are beneficial to the formation of ethylene. Furthermore, time-on-stream analysis was performed after 13 h (Fig. 6). The selectivity of all the catalysts keeps stable at low conversion. However at high conversion, the selectivity of these four catalysts changes. Ni–Cu/CeO$_2$-NP retains 52.1% selectivity, while apparent decreases in selectivity are found for Ni–Cu/CeO$_2$-CV (from 60.5% to 17.4%), Ni–Cu/CeO$_2$-NC (from 46.2% to 13.9%) and Ni–Cu/CeO$_2$-NR (from 56.7% to −2.6%), revealing better stability of Ni–Cu/CeO$_2$-NP.

To extend the application of this series of catalysts, the catalytic properties were tested in liquid phase hexyne hydrogenation (Fig. 7). For Ni–Cu/CeO$_2$-CV and Ni–Cu/CeO$_2$-NR, the reactant is not fully converted after 7 h reaction, whereas the polyhedron and cube supported Ni–Cu bimetallic catalysts exhibit almost full conversion. The TOF of Ni–Cu/CeO$_2$-NP is 23.35 h^{-1}, two-fold higher than those of the other materials, indicating remarkable catalytic activity. A much smaller Ea value of 42.9 kJ mol^{-1} for Ni–Cu/CeO$_2$-NP based on the Arrhenius equation (Fig. 7F) demonstrates the key role of the different structures in determining the activity. It is worth noting that Ni–Cu/CeO$_2$-NC facilitates over-hydrogenation at the full conversion, leading to lower selectivity (32.6%). However, as expected, hexene is the dominant product over the CeO$_2$-NP supported NiCu alloy even at high conversion. The above results basically reflect that Ni–Cu/CeO$_2$-NP positively contributes to both activity and selectivity, regardless of the phase in which the reactant is present.

Insight into the activity, selectivity and stability of NiCu/CeO$_2$-NP

As the vital rate-determining step for semi-hydrogenation of alkynes,[43] the adsorption and activation of hydrogen should be considered. By analyzing the results of H$_2$ chemisorption (Fig. S17 and Table S9†), the maximum adsorption capacity over Ni–Cu/CeO$_2$-NP is estimated to be 33 cm^3 g^{-1}, more than 1.5-fold higher in comparison to the others, illustrating the superior adsorption ability. Interestingly, relative to the close metal dispersions in the different samples, the large differences in hydrogen chemisorption may suggest the existence of hydrogen spillover. To further confirm the speculation, we calculated the ratio of H/metal (Ni and Cu, both of which are considered to be reasonable adsorbed sites for H$_2$ under these test conditions) according to the H$_2$ adsorption capacity. The results in Table S9† show that the ratios of H atoms to total metal atoms of all the samples exceed 1, but the degree of this suggests the different ability of hydrogen spillover over the four catalysts. Specifically, the H/metal ratio of NiCu/CeO$_2$-NP is 2.6, much higher than those of NiCu/CeO$_2$-CV (1.1), NiCu/CeO$_2$-NC (1.9) and NiCu/CeO$_2$-NR (1.3), indicating that this sample exhibits the most significant hydrogen spillover effect. Additionally, since CeO$_2$ could be regarded as an active support due to the spillover effect, the total active surface areas were also determined based on the hydrogen chemisorption, and the calculated equation is as:

$$S = \frac{V_H}{V_m} \times N_A \times S_H,$$

where V_H is the H$_2$ adsorption capacity, V_m is the molar volume of gas, N_A is Avogadro's constant, and S_H is the surface area occupied by one hydrogen atom (0.065 nm^2). As expected, the results in Table S9† indicate that NiCu/CeO$_2$-NP also exhibits the highest active surface area due to the obvious hydrogen spillover. In terms of TPD profiles (Fig. S18†), the peak at above 100 °C ascribed to the chemisorbed hydrogen desorption in Ni–Cu/CeO$_2$-NP remarkably moves to lower temperature relative to that of Ni–Cu/CeO$_2$-NC, Ni–Cu/CeO$_2$-NR and Ni–Cu/CeO$_2$-CV, indirectly reflecting that more easier H$_2$ activation/dissociation occurs on the NiCu nanoalloy. By combination of
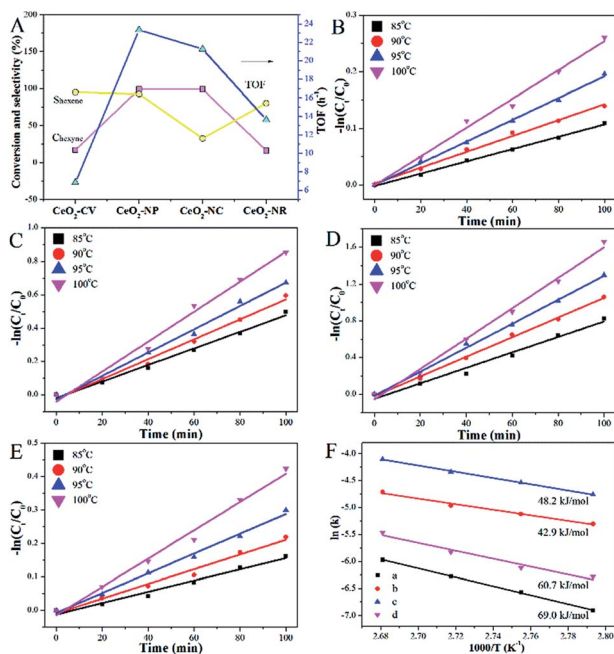

Fig. 7 (A) Performance in liquid reaction (TOF estimated at 2 h); (B–E) −ln(C_t/C_0) − dt plots at different temperatures; (F) Arrhenius plots for CeO$_2$-CV (a), CeO$_2$-NP (b), CeO$_2$-NC (c) and CeO$_2$-NR (d) supported Ni–Cu samples (0.05 g of catalysts; 0.005 mol of 1-hexyne; 10 mL of toluene as solvent).

chemisorption with TPD, the improvement of activity is clearly understood.

Fig. 8 presents IR spectra during hydrogenation of acetylene over NiCu catalysts. The range of 3500–2700 cm^{-1} is chosen to focus on the C–H modes given the absence of ν(C≡C) vibrational features due to the surface selection rule.[44] Besides, considering the clear distinction between Ni–Cu/CeO$_2$-NP and Ni–Cu/CeO$_2$-NC (the structure, electronic perturbation or catalytic behaviour), these two materials were selected as targets. As a comparison, the same experiment was executed on the pristine ceria, in which no obvious peak originating from chemically adsorbed species can be observed (Fig. S19†). Therefore, the peak at *ca.* 3236 cm^{-1} in the spectra of NiCu catalysts should be ascribed to the weak adsorption of acetylene in the π- or di-σ-complex.[45]

However, the unambiguous identification of the relative coverages of π- and di-σ-bonded acetylene could not be executed due to the wide peak caused by overlap. When hydrogen is introduced, the peaks in the range of 3100–2900 cm^{-1} assigned to CH$_2$ symmetric stretching become visible, demonstrating that selective hydrogenation of acetylene mainly produces ethene over Ni–Cu/CeO$_2$-NP.[46] However, in the case of Ni–Cu/CeO$_2$-NC (Fig. 8B), the peaks arising at 2962 cm^{-1}, 2812 cm^{-1}, 2835 cm^{-1} and 2881 cm^{-1} correspond to CH$_3$ and CH$_2$ asymmetric stretching, illustrating deep hydrogenation to ethane. This is correlated exactly with π-bonded acetylene as weaker adsorption, which is generally beneficial to inhibit over-hydrogenation compared with the di-σ-bonded acetylene. Accordingly, to achieve the proportion of the π- and di-σ-bonded mode, C$_2$H$_4$-IR is performed due to the overlap in the spectra of acetylene. The IR spectra of ethene on the target materials exhibit four peaks assigned to v (C–H) and vs (C–H) of π-bonded and di-σ-bonded ethene, respectively (Fig. 8C). The higher ratio of π- to di-σ-bonded ethene in the catalyst with the

nanopolyhedron indicates that C$_2$H$_4$ prefers to adsorb on the active atoms in the π configuration with a low adsorption energy. Moreover, the reducible CeO$_x$ adjacent to metal sites at the interface results in the relative increase of electron density of Ni as affirmed by EXAFS, XPS (Fig. 5) and *in situ* CO-IR experiments (Fig. 8D). The electron-rich Ni promotes ethene desorption from the catalyst surface. This is confirmed by the heat of C$_2$H$_4$ adsorption over Ni–Cu/CeO$_2$-NP (62 kJ mol^{-1}), lower than that of Ni–Cu/CeO$_2$-CV (73 kJ mol^{-1}), Ni–Cu/CeO$_2$-NR (79 kJ mol^{-1}) and Ni–Cu/CeO$_2$-NC (90 kJ mol^{-1}) in Fig. S20,† and hence enhances the selectivity of the desired product. Additionally, the presence of CeO$_x$ adjacent to the metal sites strongly anchors the metal nanoparticles, and thus hinders the aggregation of alloy nanoparticles, which remain with unchanged sizes in the range of 2–3 nm (Fig. S21†).

More importantly, no noticeable change is observed in bulk structures and surface composition of the polyhedron supported NiCu alloy catalyst, as confirmed by STEM, XRD and XPS analysis; that is, the nanoalloy structure is very stable (Fig. 9). This is due to the fact that the interface of metal–ceria is formed in the process of reduction which acts equally on the Ni and Cu in the alloy, and is responsible for the preferable stability.

Based on the above results, a possible mechanism considering the alloying and interfacial effect of Ni–Cu/CeO$_2$ catalysts for the selective hydrogenation of alkynes is proposed (Scheme 2). Relative to CeO$_2$-NC and CeO$_2$-NR, nanopolyhedron (NP) ceria leads to the generation of homogeneous Ni–Cu nanoalloys, owing to the equivalent interactions of Ni and Cu species
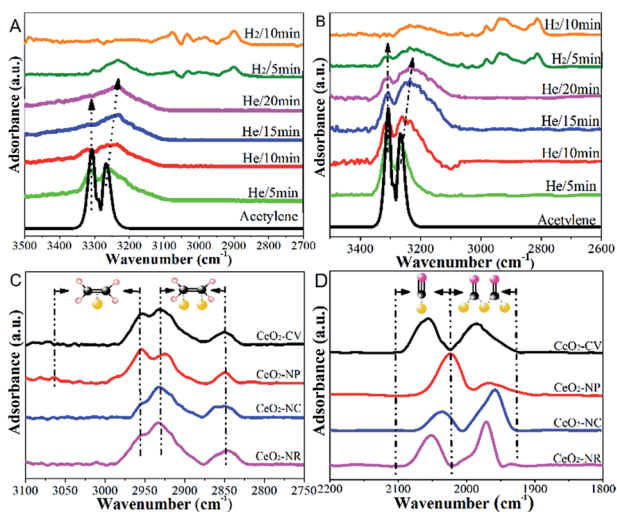

Fig. 8 *In situ* FTIR spectra of acetylene exposed to: (A) Ni–Cu/CeO$_2$-NP and (B) Ni–Cu/CeO$_2$-NC. (C) *In situ* FTIR spectra of ethylene adsorption (D) CO-IR on Ni–Cu/CeO$_2$ catalysts (pink: H; black: C; yellow: NiCu alloy; dark pink: CO).
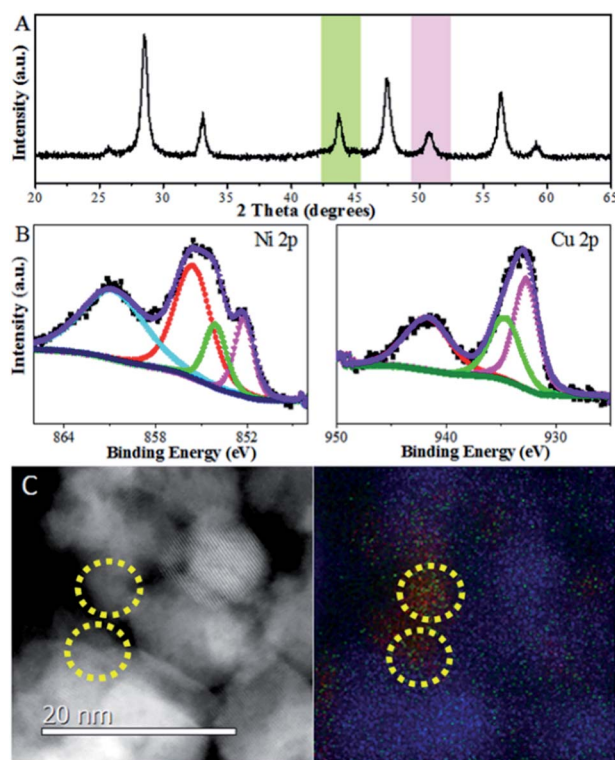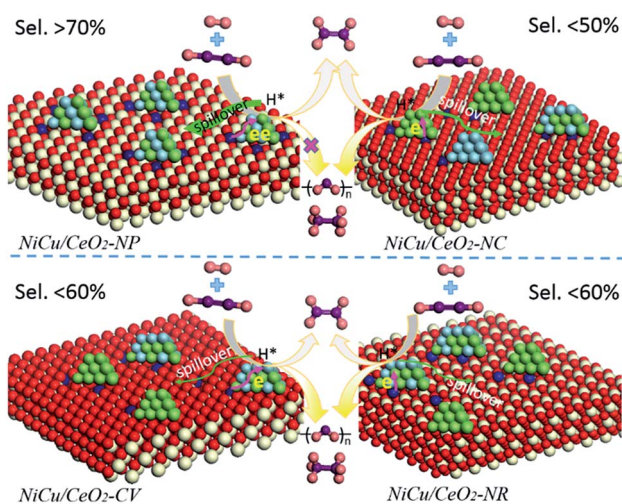

Fig. 9 (A) XRD profiles, (B) XPS spectra, and (C) STEM images of spent Ni–Cu/CeO$_2$-NP after 13 h of usage (red: Ni; green: Cu).

Scheme 2 Schematic illustration of the reaction for CeO₂-CV, CeO₂-NP, CeO₂-NC and CeO₂-NR supported Ni–Cu catalysts (white: Ce^{4+}; dark blue: Ce^{3+}; red: O; green: Ni; blue: Cu; dark pink: H; purple: C).

with CeO₂ (111) facets. Although the (111) facet is also observed in CeO₂-CV, the relative proportion is lower than that of CeO₂-NP, and thus the corresponding catalyst exhibits a low alloying degree. In the process of reaction, the NiCu/CeO₂-NP catalyst with homogenous NiCu alloy structure exhibits a significant hydrogen spillover effect, which leads to the increase of active surface area, and thus contributes to enhanced activity. More importantly, the presence of CeOₓ adjacent to metal sites at the interface in the NiCu/CeO₂-NP not only favors the generation of electron-rich Ni atoms which facilitate the desorption of ethene, but also results in excellent stability of the alloy structure. However, this kind of CeOₓ adjacent to the NiCu alloy structure is difficult to observe in CeO₂-CV, CeO₂-NC and CeO₂-NR systems.

Conclusions

In summary, we first explore and put forward the support morphology/facet-dependent alloying behaviour as well as interfacial effects. In detail, a series of CeO₂ materials with nanopolyhedron (NP), nanorod (NR), nanocube (NC) and conventional polycrystalline (CV) shapes were fabricated and used as supports to achieve environmentally benign non-noble Ni–Cu catalysts by conventional impregnation. As confirmed by the XRD and Cs-corrected STEM, the ceria with a polyhedron structure mainly involving (111) facets contributed to the formation of a homogenous and stable NiCu alloy which exists in intimate contact with CeOₓ at the interface, whereas Ni–Cu/CeO₂-NR and Ni–Cu/CeO₂-CV, particularly Ni–Cu/CeO₂-NC induced a low extent of alloying with partial monometallic Ni and Cu being present. The nature of substrate morphology inducing the structure of active metal was attributed to the comparative interaction of Ni and Cu species with CeO₂ (111) facets which expose relatively few low coordination sites, as confirmed by XRD, PAS, XAS, methanol-IR and XPS. Moreover, excellent catalytic behaviour for selective hydrogenation of

acetylene and hexyne was obtained over the homogeneous NiCu alloy on the nanopolyhedron ceria. The improved activity was attributed to the promotion of hydrogen activation/dissociation. A consequence of favorable adsorption mode for acetylene and weak adsorption of the resulting ethene product originating from the isolated electron-rich Ni atoms in the NiCu alloy contributed to the excellent selectivity. More importantly, the preferable stability is due to the suitable interfacial effect; that is, the reconstructed interfaces with the presence of CeOₓ species adjacent to the metal sites in the interface act equally on the Ni and Cu in the alloy, anchoring the alloy nanoparticles, and meanwhile inhibiting the separation of Cu from Ni atoms.

Experimental section

Materials

All chemical reagents, including $Ni(NO_3)_2 \cdot 6H_2O$, $Ce(NO_3)_3 \cdot 6H_2O$, $Na(OH)_2$ and $Cu(NO_3)_2 \cdot 3H_2O$ were bought from Aladdin. Deionized water was employed in the experiment.

Synthesis of supports and the corresponding catalysts

The fabrication of CeO₂ with different morphologies was similar to a previous paper.[15] For CeO₂-NP, CeO₂-NC and CeO₂-NR, 0.3300 g, 16.8000 g and 0.3300 g NaOH was dropped into 40 mL Ce(NO₃)₃ solution (1.9621 g) with stirring at 25 °C for 30 min, followed by aging at 180 °C, 180 °C and 100 °C for 24 h in a 100 mL stainless steel autoclave, respectively. The white precipitate was washed and dried at 60 °C overnight. And then a calcination process using a muffle was carried out at 500 °C for 4 h to obtain the final products. The conventional polycrystalline CeO₂ was only derived by calcination of Ce(NO₃)₃·6H₂O under the above conditions in the oven. All the NiCu catalysts with a Ni and Cu loading of 5.00 wt% were synthesized by impregnation. In detail, 0.60 g of support was suspended in 10 mL aqueous solution containing $Ni(NO_3)_2 \cdot 6H_2O$ and $Cu(NO_3)_2 \cdot 3H_2O$ solution with a mole ratio of 1 : 1 for 4 h with stirring, followed by drying at 60 °C for 12 h and calcination at 500 °C for 4 h, and were denoted as Ni–Cu/CeO₂-NP-Pre, Ni–Cu/CeO₂-NR-Pre, Ni–Cu/CeO₂-NC-Pre and Ni–Cu/CeO₂-CV-Pre. All calcined precursors were reduced in H₂/Ar at 500 °C for 4 h and cooled down slowly to room temperature. Notably, when the temperature decreases to 100 °C, the samples are treated using a mixture of diluted oxygen with nitrogen (3% O₂/N₂) in case re-oxidation results in the change of structure. The catalysts were named as Ni–Cu/CeO₂-NP, Ni–Cu/CeO₂-NR, Ni–Cu/CeO₂-NC and Ni–Cu/CeO₂-CV, respectively.

Characterization of samples

X-ray diffraction (XRD) patterns were recorded using a Shimadzu XRD-6000 diffractometer using copper radiation (Kα1 = 0.154 nm) with a rate of 0.5° min⁻¹. To investigate the concentration/type of oxygen vacancies, PAS using a fast–slow coincidence ORTEC system (a time resolution of 187 ps for the full width at half maximum) and Raman measurements using a 532 nm laser were conducted. X-ray photoelectron spectra (XPS) were collected using a Thermo VG ESCALAB 250

spectrometer equipped with an Al Kα anode, and the calibration peak is the C 1s peak at 284.6 eV. Metal dispersion was estimated by CO chemisorption based on a Ni/CO ratio of 1 using a Micromeritics ChemiSorb 2720. A temperature-programmed process (TPx) was also carried out on this instrument. 0.1 g of sample was degassed in Ar at 200 °C for 1 h and reduced under H₂/Ar at 30–500 °C. Cs-corrected STEM images were obtained on a JEOL ARM200F microscope equipped with a probe-forming spherical-aberration corrector. The extended X-ray Absorption Fine Structure (EXAFS) was analysed at the 1W1B beamline of Beijing Synchrotron Radiation Facility (BSRF). The typical energy of the storage ring was 2.5 GeV with a maximum current of 250 mA. *In situ* diffuse reflectance infrared Fourier transform (DRIFT) spectroscopy of C_2H_2 and C_2H_4 was performed on a Bruker Tensor 27 instrument. The samples were pre-treated in H₂/Ar at 500 °C for 30 min, followed by recording a background with a resolution of 4 cm^{-1}. Then, the catalysts were exposed to C_2H_2 or C_2H_4 for 30 min, and purged with He before the collection of spectra. CH₃OH-IR was performed on a Bruker Tensor 27 instrument. The samples were pre-treated in He at 300 °C for 30 min, followed by recording a background with a resolution of 4 cm^{-1}. Then, CeO_2 was exposed to CH₃OH vapor through He bubbling for 30 min, and purged with He before collection of spectra.

Catalytic testing

The gas-phase reaction was performed in a quartz-bed reactor using 100 mg of catalyst diluted with SiC. The catalysts were reduced in 10% H₂/N₂ at 300 °C for 2 h prior to catalytic testing, and then determined in a mixture of 0.6% C_2H_2/5.4% C_2H_4/balance N₂. Gas compositions were analysed using a gas chromatograph (PE Clarus 580) connected to a flame ionization detector (GC-FID) using an elite alumina capillary column. Conversion was denoted as the amount of reacted acetylene divided by the amount introduced. Selectivity to the product was calculated as the amount formed divided by the amount of acetylene reacted. Oligomers were evaluated based on carbon balance. Liquid-phase hydrogenation of hexyne was performed in a 25 mL reactor of a semi-batch stainless steel reactor with a quartz tank inside. Each reactor was charged with samples (50 mg), 1-hexyne (0.005 mol) and toluene as solvent (10 mL). Reaction products were monitored off-line through a GC-FID with a DB-Wax column ($d_f = 0.250$ μm, 30 m × 0.320 mm). The carbon balance was within ±5%.

Conflicts of interest

There are no conflicts to declare.

Acknowledgements

Notes and references

1 R. Ferrando, J. Jellinek and R. L. Johnston, *Chem. Rev.*, 2008, **108**, 846–904.

2 D. S. Wang and Y. D. Li, *Adv. Mater.*, 2011, **23**, 1044–1060.

3 W. G. Menezesa, L. Altmann, V. Zielasek, K. Thiel and M. Bäumer, *J. Catal.*, 2013, **300**, 125–135.

4 D. L. Li, M. M. Lu, K. Aragaki, M. Koike, Y. Nakagawab and K. Tomishige, *Appl. Catal., B*, 2016, **192**, 171–181.

5 B. Seemala, C. M. Cai, C. E. Wyman and P. Christopher, *ACS Catal.*, 2017, **7**, 4070–4082.

6 J. Jones, H. F. Xiong, A. T. DeLaRiva, E. J. Peterson, H. Pham, S. R. Challa, G. S. Qi, S. Oh, M. H. Wiebenga, X. I. P. Hernández, Y. Wang and A. K. Datye, *Science*, 2016, **353**, 150–154.

7 G. Vilé, S. Colussi, F. Krumeich, A. Trovarelli and J. Pérez-Ramírez, *Angew. Chem.*, 2014, **126**, 12265–12268.

8 F. Dvorak, M. Farnesi Camellone, A. Tovt, N. D. Tran, F. R. Negreiros, M. Vorokhta, T. Skala, I. Matolinova, J. Myslivecek, V. Matolin and S. Fabris, *Nat. Commun.*, 2016, **7**, 10801.

9 S. Mclntosh and R. J. Gorte, *Chem. Rev.*, 2004, **104**, 4845–4866.

10 J. W. Yoon, J. S. Kim, T. H. Kim, Y. J. Hong, Y. C. Kang and J. H. Lee, *Small*, 2016, **12**, 4229–4240.

11 A. Trovarelli and J. Llorca, *ACS Catal.*, 2017, **7**, 4716–4735.

12 J. A. Rodriguez, D. C. Grinter, Z. Liu, R. M. Palomino and S. D. Senanayake, *Chem. Soc. Rev.*, 2017, **46**, 1824–1841.

13 N. J. Lawrence, J. R. Brewer, L. Wang, T. S. Wu, J. Wells-Kingsbury, M. M. Ihrig, G. H. Wang, Y. L. Soo, W. N. Mei and C. L. Cheung, *Nano Lett.*, 2011, **11**, 2666–2671.

14 J. Carrasco, G. Vilé, D. Fernández-Torre, R. Pérez, J. Pérez-Ramírez and M. V. Ganduglia-Pirovano, *J. Phys. Chem. C*, 2014, **118**, 5352–5360.

15 R. Si and M. Flytzani-Stephanopoulos, *Angew. Chem., Int. Ed.*, 2018, **47**, 2884–2887.

16 L. Soler, A. Casanovas, A. Urrich, I. Angurell and J. Llorca, *Appl. Catal., B*, 2016, **197**, 47–55.

17 Y. Lin, Z. NWu, J. Wen, K. Ding, X. Yang, K. R. Poeppelmeier and L. D. Marks, *Nano Lett.*, 2015, **15**, 5375–5381.

18 N. Ta, J. J. Liu, S. Chenna, P. A. Crozier, Y. Li, A. Chen and W. Shen, *J. Am. Chem. Soc.*, 2012, **134**, 20585–20588.

19 J. C. Gonzalez, J. C. Hernandez, M. Lopez-Haro, E. del Rio, J. J. Delgado, A. B. Hungria, S. Trasobares, S. Bernal, P. A. Midgley and J. J. Calvino, *Angew. Chem., Int. Ed.*, 2009, **48**, 5313–5315.

20 M. Tinoco, S. Fernandez-Garcia, M. Lopez-Haro, A. B. Hungria, X. Chen, G. Blanco, J. A. Perez-Omil, S. E. Collins, H. Okuno and J. J. Calvino, *ACS Catal.*, 2015, **5**, 3504–3513.

21 F. Esch, S. Fabris, L. Zhou, T. Montini, C. Africh, P. Fornasiero, G. Comelli and R. Rosei, *Science*, 2005, **309**, 752–755.

22 S. Chang, M. Li, Q. Hua, L. Zhang, Y. Ma, B. Ye and W. Huang, *J. Catal.*, 2012, **293**, 195–204.

23 M. Zabilskiy, P. Djinovic, E. Tchernychova, O. P. Tkachenko, L. M. Kustov and A. Pintar, *ACS Catal.*, 2015, **5**, 5357–5365.

24 J. Liu, *ACS Catal.*, 2017, **7**, 34–59.

25 H. B. Liao, A. Fisher and Z. C. J. Xu, *Small*, 2015, **11**, 3221–3246.

26 Y. Z. Xiang, R. Barbosa and N. Kruse, *ACS Catal.*, 2014, **4**, 2792–2800.

27 S. Y. Lee, N. Jung, J. Cho, H. Y. Park, J. Ryu, I. Jang, H. J. Kim, E. Cho, Y. H. Park, H. C. Ham, J. H. Jang and S. J. Yoo, *ACS Catal.*, 2014, **4**, 2402–2408.

28 C. Herring, *Phys. Rev.*, 1951, **82**, 87–93.

29 C. W. Yang, X. J. Yu, S. Heißler, A. Nefedov, S. Colussi, J. Llorca, A. Trovarelli, Y. M. Wang and C. Wöll, *Angew. Chem., Int. Ed.*, 2017, **56**, 375–379.

30 A. Badri, C. Binet and J. C. Lavalley, *J. Chem. Soc., Faraday Trans.*, 1997, **93**, 1159–1168.

31 Z. L. Wu, M. J. Li, D. R. Mullins and S. H. Overbury, *ACS Catal.*, 2012, **2**, 2224–2234.

32 L. D. Rogatis, T. Montini, B. Lorenzut and P. Fornasiero, *Energy Environ. Sci.*, 2008, **1**, 501–509.

33 Z. L. Yuan, L. Wang, J. H. Wang, S. X. Xia, P. Chen, Z. Y. Hou and X. M. Zheng, *Appl. Catal., B*, 2011, **101**, 431–440.

34 E. T. Saw, U. Oemar, X. R. Tan, Y. Du, A. Borgna, K. Hidajat and S. Kawi, *J. Catal.*, 2014, **314**, 32–46.

35 Z. Hu, X. F. Liu, D. M. Meng, Y. Guo, Y. L. Guo and G. Z. Lu, *ACS Catal.*, 2016, **6**, 2265–2279.

36 A. Hornésa, M. Fernández-García, A. Guerrero-Ruizb and A. Martínez-Arias, *Appl. Catal., B*, 2012, **111–112**, 96–105.

37 C. Yang, X. Yu, S. Heissler, A. Nefedov, S. Colussi, J. Llorca, A. Trovarelli, Y. Wang and C. Woll, *Angew. Chem., Int. Ed.*, 2017, **56**, 375–379.

38 F. Wang, S. He, H. Chen, B. Wang, L. R. Zheng, M. Wei, D. G. Evans and X. Duan, *J. Am. Chem. Soc.*, 2016, **138**, 6298–6305.

39 A. J. McCue, C. J. McRitchie, A. M. Shepherd and J. A. Anderson, *J. Catal.*, 2014, **319**, 127–135.

40 G. Vilé, B. Bridier, J. Wichert and J. Pérez-Ramírez, *Angew. Chem., Int. Ed.*, 2012, **51**, 8620–8623.

41 D. Albani, M. Capdevilla-Cortada, G. Vilé, S. Mitchell, O. Martin, N. López and J. Pérez-Ramírez, *Angew. Chem.*, 2017, **56**, 10755–10760.

42 A. J. McCue, A. Guerrero-Ruiz, C. Ramirez-Barria, I. Rodríguez-Ramos and J. A. Anderson, *J. Catal.*, 2017, **355**, 40–52.

43 Y. N. Liu, J. Zhao, J. T. Feng, Y. F. He, Y. Y. Du and D. Q. Li, *J. Catal.*, 2018, **359**, 251–260.

44 Y. D. Chen, C. M. Li, J. Y. Zhou, S. T. Zhang, S. He, M. Wei, D. G. Evans and X. Duan, *ACS Catal.*, 2015, **5**, 5756–5765.

45 M. A. Albiter and F. Zaera, *Langmuir*, 2010, **26**, 16204–16210.

46 J. Wood, M. J. Alldrick, J. M. Winterbottom, E. H. Stitt and S. Bailey, *Catal. Today*, 2007, **128**, 52–62.